LCPOM: Precise Reconstruction of Polarized Optical Microscopy Images of Liquid Crystals

Chuqiao Chen,[†,‖] Viviana Palacio-Betancur,[†,‖] Sepideh Norouzi,[‡] Pablo F. Zubieta-Rico,[†] Nina Chang,[†] Monirosadat. Sadati,[‡] Stuart J. Rowan,[¶,†] and Juan J. de Pablo[*,†,§]

†*Pritzker School of Molecular Engineering, University of Chicago, Chicago, IL 60637, USA*

‡*Department of Chemical Engineering, University of South Carolina, Columbia, SC 29208, USA*

¶*Department of Chemistry, University of Chicago, Chicago, IL 60637, USA*

§*Center for Molecular Engineering, Argonne National Laboratory, Lemont, IL 60439, USA*

‖*These authors contributed equally.*

E-mail: depablo@uchicago.edu

Abstract

When examined with polarized optical microscopy(POM), liquid crystals display interference colors and complex patterns that depend on the material's microscopic orientation. That orientation can be manipulated by application of external fields, a feature that provides the basis for applications in optical display and sensing technologies. The color patterns themselves have a high information content. Traditionally, however, calculations of the optical appearance of liquid crystals have been performed by assuming that a single-wavelength light source is employed, and reported on a monochromatic scale. In this work, the original Jones matrix method is extended to

calculate the colored images that arise when a liquid crystal is exposed to a multi-wavelength source. By accounting for the material properties, including the local orientation, the visible light spectrum, and the CIE (International Commission on Illumination) color matching functions, we demonstrate that the proposed approach produces colored POM images that are in quantitative agreement with experimental data. Results are presented for a variety of systems, including radial, bipolar, and cholesteric droplets, where results of simulations are compared to experimental images. The effects of droplet size, topological defect structure, and droplet orientation are examined systematically. The technique introduced here generates images that can be directly compared to experiments, thereby facilitating machine learning efforts aimed at interpreting LC microscopy images, and paving the way for the inverse design of materials capable of producing specific internal microstructures in response to external stimuli.

Keywords

liquid crystals, polarized optical microscopy, simulation, data-driven, image analysis

Introduction

When confined between a pair of linear polarizers, liquid crystals (LCs) can display a wide range of interference colors and complex patterns owing to the material's optical birefringence (*i.e.* the difference between refractive indices parallel and perpendicular to the director).[1,2] The brightness and color hues are sensitive to the local molecular order, which can be controlled through external stimuli, including electric fields, magnetic fields, flows, chemical cues and temperature.[1–4] On account of their responsive nature and large optical birefringence, LCs are widely used in optical devices, ranging from mature technologies such as liquid crystal displays to state-of-the-art sensors that can detect toxins, biomolecules, and

microplastics.[5–10]

Liquid crystals are generally characterized using polarized optical microscopy (POM), which provides a direct measure of the material's alignment and and is able to identify any misalignment that might arise in a sample.[8,11–15] The alignment can be described by the director ($\mathbf{n}$) which is a vector field indicating the mean-field average direction of the LC molecules local to its spatial coordinate ($\mathbf{r}$). In confined LC systems, large spatial distortions in the order field can develop on account of the incompatibility between surface and bulk orientations, leading to distinct POM images. The realignment of a confined LC can be triggered by altering the balance between elastic and surface energies; a minute change in the external environment can completely change the material's appearance under POM.[11,16,17] Sensing and display devices often rely solely on the transition between configurations that exhibit different topological defects (such as bipolar and radial), which are identifiable through the brightness profile. The substantial color changes that accompany such transitions are rarely exploited.[15,18] Understanding how the POM color patterns of LCs correspond to a particular molecular alignment is of interest not only from a fundamental perspective, but also for development of next-generation optical and sensing devices.[19,20]

One method to understand the color texture of POM images is to rely on the Michel-Levy chart, which tabulates the interference color as a function of thickness and birefringence.[21–23] That method, however, is limited to a uniform orientation of the director field, and is incapable of predicting the interference color in confined geometries where the alignment exhibits large spatial variations. In addition, the POM images can change with light sources and viewing angles, making it difficult to match the color patterns with the underlying order field and hindering comparisons to experiments with different setups.

More generally, POM images are calculated without color information using the Ondris-Crawford method, which produces the brightness profile corresponding to the LC order field.[24–26] In this method, the sample is first discretized into layers whose thickness is much smaller than the wavelength. Subsequently, the propagation of light is modeled by mul-

tiplying the Jones matrix of each layer, which computes the retardation according to the local LC alignment. The method is versatile and easy to implement. It has been applied to many geometries, including droplets and toroids, where it is possible to reproduce the brightness profile of both nematic and cholesteric LCs.[17,25–28] The Ondris-Crawford method can be viewed as the standard approach for comparisons between experimental POM images and model predictions with numerical simulations.[11,13,17,29–32] A major limitation, however, is that the original formulation assumes a single wavelength, and it is difficult to compare a monochromatic brightness profile with the color images that are typically obtained from a white light source with a distribution of wavelengths in the range between 400-680nm. Note that the effect of having a broadband light source has been discussed in several experimental and simulation studies, but reports that include simulated colored POM images are limited.[28–31,33,34] An exception is provided by the work of Yoshioka *et al.*, who presented several colored POM images from calculations that showed good agreement with experiments.[35] Unfortunately, few details regarding the calculation of the color images were provided in that report. The colored POM images in many other reports demonstrate clear visual discrepancies compared to experimental images, likely due to simplified assumptions of the material optical properties or the RGB signal conversion process. While the underlying physics of obtaining POM images are well-known, an accurate simulation of colored POM images requires the proper considerations of nuanced material properties and the basic knowledge of color science.

In this work, we present a systematic methodological study of the computational generation of POM images (and an accompanying software package), which is validated through quantitative comparisons to experimental data for a variety of systems. The colored POM images are calculated by introducing a color matching function that combines the information corresponding to multiple wavelengths to produce RGB values equivalent to the colors perceived by the human eye.[36–39] In addition, we take into consideration the emission spectrum of the light source, the dependency of refractive indices on wavelength, and the reflection at

the droplet interface. The accuracy and the applicability of our method are demonstrated by comparing simulated and experimental POM images of radial, bipolar, and cholesteric droplets. Lastly, we demonstrate that one can extract meaningful physical properties of the nematic phase from the color information, enabled by the accurate dataset generated from the simulations. We anticipate that the open-access LCPOM Python package developed in this work will facilitate experimental and theoretical research efforts aimed at designing advanced LC-based materials.

Methods of calculating colored POM micrographs

When colored POM images are captured in the laboratory, the sample is typically illuminated with a white light that has a non-uniform spectrum distribution. The light spectrum differs between laboratories and can alter the color texture.[40] To produce an accurate color image, the LED spectrum $I(\lambda)$ for experimental images produced in this work is obtained from the manufacturer or measured by an optical spectrometer. (Figure 1A-B and Supplementary Fig. S1) In the calculations presented below, the light spectrum (400 nm - 680 nm) is discretized into $N_\nu = 20$ intervals and the intensity profile for each wavelength is computed using the Ondris-Crawford method.[25,26] The order field configurations are obtained either from analytical or numerical solutions, which are then interpolated onto a regular grid with the desired resolution. Each of the single-wavelength intensity profiles depends on the local LC alignment and the optical birefringence (Δn). (Figure 1A) It is important to note that Δn is not a single constant, but a function of the wavelength (λ) and the order parameter S (which is a function of temperature and spatial gradient). Overall, both the ordinary and extraordinary refractive indices (n_o and n_e respectively) decrease with wavelength and saturate in the near-IR region. The quantitative relationship can be described by a three-band model with constants fitted to experimental measurements.[4,41] (Figure 1C, see Supplementary Materials for the relevant equations).

In confined droplets, the director field is distorted and the local order parameter S is smaller near the topological defects, leading to a drop in the local birefringence Δn. Based on the Vuks equation, here we assume that $\Delta n \propto S$ where S may be taken as constant in simple analytical director fields (such as the radial hedgehog), or contains spatial variations informed by numerical simulations. For derivation and experimental validation of the Vuks relation, see Horn (1978) and Li and Wu (2004).[42,43] The local Δn, n_e and n_o values are given by:

$$\Delta n(S) = \Delta n(S_r)\frac{S}{S_r} \tag{1}$$

$$n_e = \langle n \rangle + \frac{2}{3}\Delta n \tag{2}$$

$$n_e = \langle n \rangle - \frac{1}{3}\Delta n \tag{3}$$

where $\langle n \rangle$ represents the average birefringence value that stays constant for a given temperature; S_r and Δn_r are the order parameter and optical birefringence of a uniform bulk taken as the reference state. For the liquid crystal 4-cyano-4'-phentylbiphenyl (5CB) considered in this work, the reference state is taken to be $S_r = 0.57$ at $T = 25.1°$. The refractive indices n_o and n_e are plotted as a function of λ for uniform alignment ($S = 0.57$) and near a topological defect ($S = 0.1$) (Figure 1C). It is worth noting that at $S = 0.57$, Δn decreases from 0.067 to 0.051 as λ increases from $0.40\mu m$ to $0.68\mu m$, which is significant enough to affect higher order interference colors; this effect has generally been ignored in previous reports.

In addition to the interference taking place in the bulk of the liquid crystal, we also consider the light transmission ratio at the water-LC interface. For simplicity, diffraction and refraction at the interface are ignored. In this study, the transmission ratio $\overline{Tr}$ is approximated from the Fresnel equation using the refractive indices of water and 5CB.[41,44] (Details are available in Supplementary materials) $\overline{Tr}$ decreases with increasing incident angle (θ_i), leading to lower brightness near the periphery of the droplet (Figure 1D).

To combine these multiple intensity profiles at different wavelengths into an RGB image,

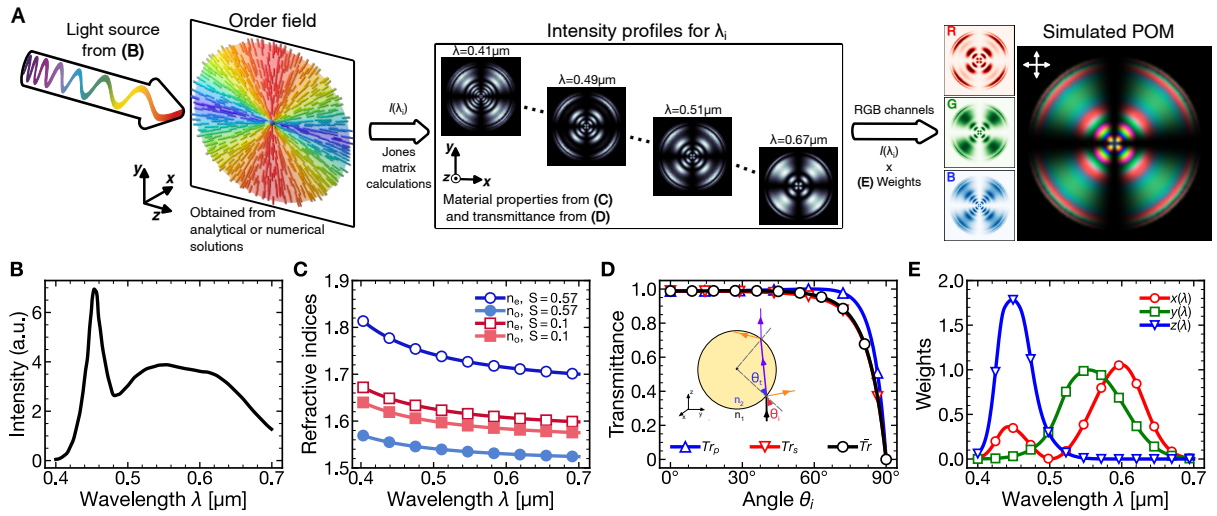

Figure 1: **Illustration of the method and plots of key physical properties.** (A) Schematic representation of the method for calculation of a colored POM image from the order field. In this illustration, a radial droplet with $d = 20\mu m$ is computed with $N_\lambda = 14$ wavelengths. The color indicates the angle between the local director and the y axis. (B) LED light spectrum obtained from the manufacturer of Zeiss Axioscope. (C) Refractive indices of 5CB as a function of order parameter S and wavelength λ obtained from a semiempircal model in literature.[4] (D) Transmission ratio as a function of incident light angle. Tr_p, Tr_s and $\overline{Tr}$ stand for transmission ratios of p-polarized, s-polarized light and the weighted average value. See Supplementary materials for details. (E) Color matching functions $x_i(\lambda)$ from the CIE 1931 standard.

we consider how humans perceive color and how color images are stored in modern electronic devices. Briefly, the human eye can sense different wavelengths of light mainly with three types of cone cells in the retina.[36] These signals are processed by an intricate neural network to generate a perception of color in the brain. Modern-day electronics represent color images by assigning tri-stimuli values such as RGB, XYZ, or HSV (Hue Saturation Value) to each pixel, so that digital displays can allow the human eye to perceive colors that are relatively independent of the device or the lighting environment. The matching functions x_i (λ) that transform wavelength signals to XYZ values were originally determined by the International Commission on Illumination (in 1931 - CIE 1931 color space), and they are still widely employed today (Figure 1E).[37,38] In this work, the intensity profiles $P(\mathbf{r}, \lambda)$ at N_λ wavelengths are weighed by the light intensity $I(\lambda)$ and the matching functions to obtain an XYZ color image which is then converted to the RGB color image by a linear transformation.[39]

The image before transformation is calculated by:

$$X_i(\mathbf{r}) = \int P(\mathbf{r},\lambda)\overline{Tr}^2(\mathbf{r},\lambda)I(\lambda)x_i(\lambda)d\lambda$$
$$\approx \sum_j^{N_\lambda} P(\mathbf{r},\lambda_j)\overline{Tr}^2(\mathbf{r},\lambda_j)w_{ij}(\lambda_j) \quad (4)$$
$$w_{ij} = \int_{\lambda_j}^{\lambda_{j+1}} I(\lambda)x_i(\lambda)d\lambda \quad (5)$$

where $\mathbf{r}$ represents the spatial coordinate; the index i indicates the color channel ($x_i(\lambda) = x(\lambda), y(\lambda)$, or $z(\lambda)$ corresponds to the weights of color matching function in Fig. 1E, distinctive from the spatial coordinates); the weight w_{ij} is computed independent of the director field and shows how much the jth wavelength contributes to the ith color channel. $P(\mathbf{r},\lambda_j)$ represents the single-wavelength intensity profiles obtained from the Ondris-Crawford method. Note that the $\overline{Tr}$ term is squared because each ray passes through the water/5CB interface twice. The formula above assumes that the droplet is illuminated with parallel rays while ignoring refraction. Alternatively, this method could be further upgraded by accounting for refraction with geometric ray-tracing methods, as demonstrated by Mur et al. (2017) for low birefringence LC.[28] Another approach to treat diffraction is discussed in Steinberg (2020), which devises analytical solutions to the Maxwell's equations in some cases.[45] The current work does not adapt ray optics simulation due to its large computational cost (slowing down the calculation by 100$\sim$ 1000 times).

In summary, the color image is obtained in four steps: 1) Generate the director field through analytical or numerical solutions and interpolate it onto a regular grid with the desired resolution. 2) Compute N_λ intensity profiles for discretized wavelengths using the Ondris-Crawford method and multiply by the transmission ratio according to the local curvature. 3) Weigh by the LED spectrum and color matching functions to get the XYZ channel images. 4) Transform the image from XYZ color space to RGB color space and represent the result as a color image.

In the following sections, we present the diverse applications of the LCPOM Python package, demonstrating its exceptional capabilities and providing benchmarks for computational tools seeking to align with experimental observations. Not only does our software serve as a convincing proof of concept, but it also offers invaluable insights into crucial considerations such as system size, treatment of topological defects, probing the orientation of nematic morphologies, and moreover, the faithful reproduction of POM images in cholesteric systems. It is noted that each image (110×110 pixels) takes less than 20 minutes to compute on a single Intel Core i5 CPU processor. The sensitivity and speed of this method can serve for generating a data-set that facilitates inverse design or machine learning.[46,47]

Effects of system size exemplified by radial droplets

To explore the effect of system size, we have generated POM images of radial droplets with various diameters ($d = 2r_0$). The radial droplet provides a canonical example of the interplay between bulk elasticity and surface orientation. In the presence of a surfactant, the LC molecules orient perpendicular to the surface of the droplet, resulting in a hedgehog defect at the center of the droplet. This particular system has been reported to be stable across a wide range of temperature, different materials, and across different length scales. The analytical description of the radial director field is $\mathbf{n} = \mathbf{x}/\left\|\mathbf{x}\right\|$. The defect is a divergence of the director field, commonly referred to as a radial hedgehog, as pictured in Figure 1A.

The LCPOM results of a radial hedgehog in Figure 2A show the progression of colors that emerge as the diameter of the LC droplets is increased from $d = 2\mu$m to 20μ. As the diameter increases from $d = 3\mu$m to 6μm, the first-order interference colors change from yellow to blue (Fig. S2). This color change can be understood by computing the optical path difference (OPD) between the ordinary and extraordinary light waves and the corresponding phase shift of the linearly polarized light (See SI for detailed analysis). At $d = 6.5\mu$m, a second color ring emerges from the center of the droplet as the maximum phase shift

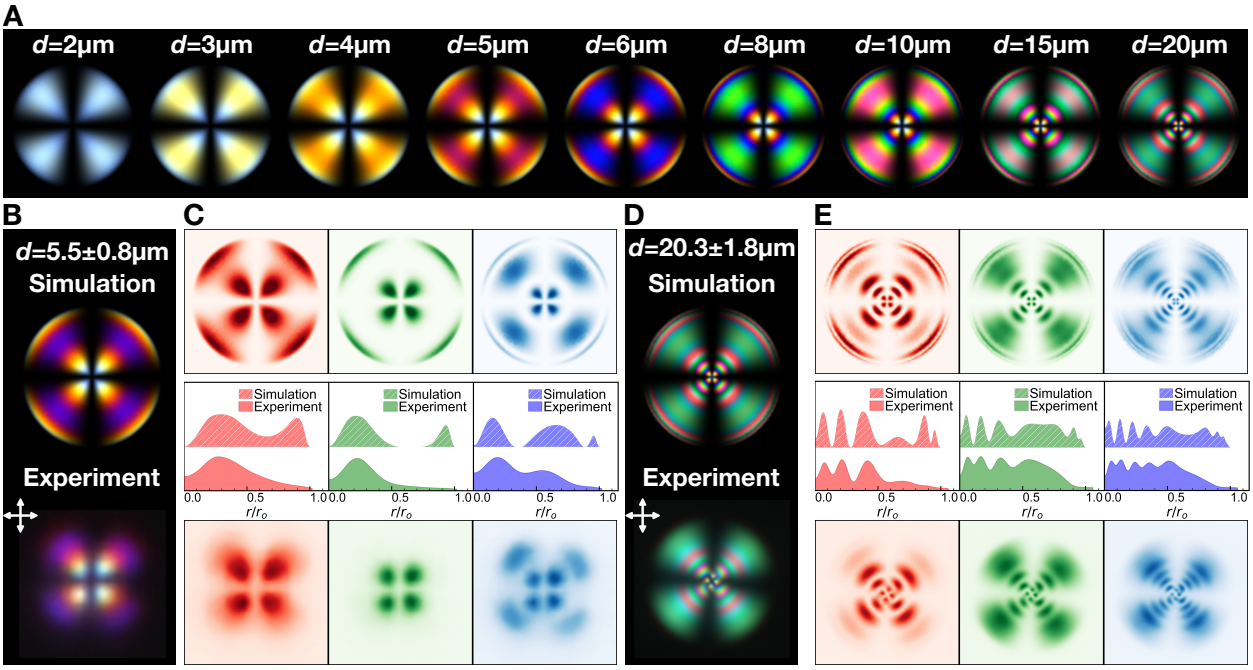

Figure 2: **Simulation of the color POM images of radial droplets from the analytical order field.** (A) Simulated images of a radial droplet from different sizes. The orientation profile is shown in Figure 1A. (B) Comparison of the image of $d = 5.5 \pm 0.8\mu$m between simulation and experiment. ($r_0 = d/2$) (C) Intensity profiles of the RGB color channels and the radial intensity profile in B. (D) Comparison of the image of $d = 20.3 \pm 1.8 \pm \mu$m between simulation and experiment. (E) Intensity profiles of the RGB color channels and the radial intensity profile in D.

exceeds 180° (Fig. S3). The simulated color textures are highly sensitive to system size, and a discrepancy in diameter as small as $0.5\mu m$ leads to notable differences in the optical appearance. This level of sensitivity is not seen in BW intensity profiles, indicating that more information about the LC order is captured by our proposed method. (Fig. S4) Moreover, this result highlights the use of a computational tool related to color to determine the size of an experimental system, or the possibility to infer the order parameter from microscopy images. More simulated POM images of this case are provided in Fig. S2.

To reproduce the color texture of experiments in simulations, the birefringence must be tuned down by 5%. This difference may have originated from multiple factors. Firstly, a frustrated alignment in curved geometries can lead to an attenuation of the optical birefringence near the interface compared to the uniform bulk samples in which the refractive indices are

measured. Secondly, some molecules such as water, surfactants and electrolytes may coexist in 5CB droplets, leading to a reduction in nematic order.[48] Finally, the droplet has a diffuse boundary on the bright-field images, and the determination of size has an average error of 14% calculated from the FWHM (full width at half maximum) of the boundary (see Fig. S6). This diffuse appearance is caused by the diffraction at the interface between materials with mismatching refractive indices.[44]

Overall, the color dependence on size in simulated images is in good agreement with experimental results (Figure 2B, D and S4). The simulated and experimental images were decomposed into their respective RGB channel contributions (Figure 2C and E). Given the symmetry of the radial structure, a quantitative comparison between simulated and experimental images can be achieved by integrating over the azimuthal angles and plotting the intensity profiles as a function of the normalized radial coordinate r/r_0. Each of the RGB intensity profiles contains contributions from the entire light spectrum and does not have a simple analytical form. Importantly, the peak positions of RGB intensity profiles agree with the ones observed in experiments for $r/r_0 < 0.8$, which leads to a precise prediction of the color ring locations, even for large droplets, which exhibit higher-order interference. On the other hand, peaks close to the boundary ($r/r_0 > 0.8$) are not observed in experiments, as the intensity decays faster towards the edge of the droplet than predicted. This is attributed to the diffraction and fluctuation at the interface which, as discussed above, are not considered in our algorithm.

Effects of the detailed structures of topological defects

The nature of the defect core is an active field of study, with implications for the assembly of colloids, active liquid crystals, and photonics. By definition, the defect core is the divergence of the vector order field, and can often be treated as a point charge. However, it has been shown theoretically and in experiments that the topological defects usually do not take

the shape of a point, but appear as a region with diminished order parameters.[16,18,49–52] Radial droplets of 5CB typically exhibit loop disclinations whose diameter is sensitive to the anchoring strength, the elastic constants (temperature), and the size of the droplet.[52–54] The exact topology of the defect and the source of fluctuations have been long-standing questions that have attracted considerable theoretical interest.[52–56] In experiments, the defect is usually small and sometimes appears as a blurry dot due to limitations in the optical resolution. In contrast to the hedgehog defect in Figure 1, a loop disclination is surrounded by a continuous variation of the director field and has lower rotational symmetry. This implies that the optical texture should reflect when a rigid body rotation of the disclination loop occurs, as previously proposed by de la Cote *et al.*[57]

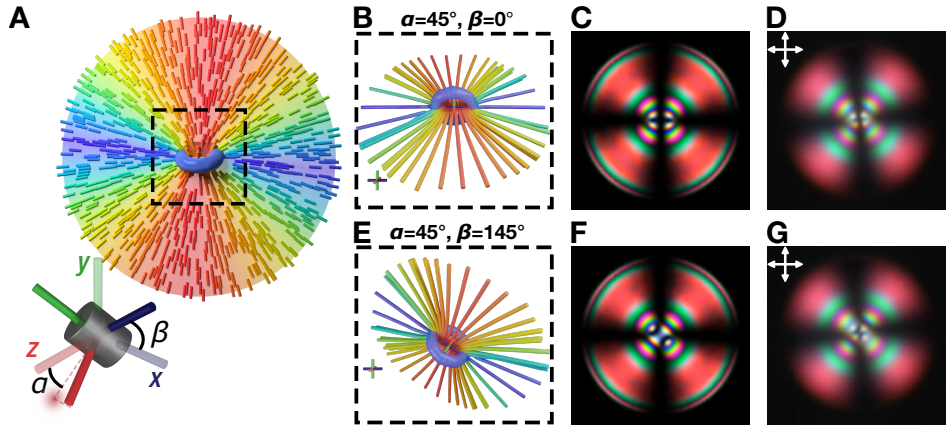

Figure 3: **Effect of loop orientation in a radial droplet.** (A) Simulated radial droplet with a disclination loop (regions with $S < 0.3$) at the center. The diameter of the loop is approximately 1.9μm. (B-C) Schematic representation of the orientation of the defect loop with $\alpha = 45°$ and $\beta = 0°$ and the corresponding simulated POM image with $d = 17.5\mu$m. (E-F) Schematic representation of the orientation of the defect loop with $\alpha = 45°$ and $\beta = 145°$ and the corresponding simulated POM image with $d = 17.5\mu$m. (D) and (G): Experimental images for $d = 17.5 \pm 1.6\mu$m.

To examine this hypothesis, we performed simulations of nematic droplets under homeotropic anchoring conditions. Calculations of the order field following a Ginzburg-Landau relaxation yield a scalar and vector order field. The simulation details can be found in the Supplementary Information. The orientations in 3D can be described by two angles, α and β, because the order fields obey the $D_{\infty h}$ symmetry. Here, α is the out-of-plane tilt angle between the

symmetry axis and the xy-plane and β represents the in-plane rotation angle between the 0-projection of the symmetry axis and the y axis (Figure 3A).

As the droplet rotates, the reorientation of the loop creates subtle but clear changes in the POM image. As expected, the image bears the highest symmetry at $\alpha = 90°$ and demonstrates more fuzzy central patterns compared to the POM image of the analytical form (Fig. S7). A distortion in the optical texture is observed when α deviates from 90° (Figure 3C-F, Supplementary Movie 1). Importantly, the simulations produce color patterns that are very similar to those observed in experiments for particular orientations of the droplet (Figure 3B-G, Supplementary Movie 2). This agreement suggests that under appropriate conditions the experiments can be directly compared to simulations to infer the orientation of the defects, thereby offering a new way of studying the dynamics and order fluctuations in confined LC environments.

Understanding micrographs of bipolar droplets through perspective sweeps

Another ubiquitous configuration in LC microemulsions is the bipolar droplet. It is characterized by two antipodal surface defects that emerge to satisfy a parallel molecular orientation tangential to the droplet's surface. The transition from a bipolar to a radial configuration can be triggered by adding a surfactant, which is the principle of operation for many LC-based sensing devices.[11] Similar to the order field in radial droplets, we performed numerical simulations to generate the vector and scalar order fields of a bipolar droplet that were then used as input for LCPOM. An advantage of this computational tool is the control over the viewpoint of an input morphology; different orientations that yield uncommon micrographs can be probed by this approach. In this case, simulated images were compared to experimental POM images of droplets created by dispersing 5CB in a PVA/water solution; additional experimental details are provided in the SI.

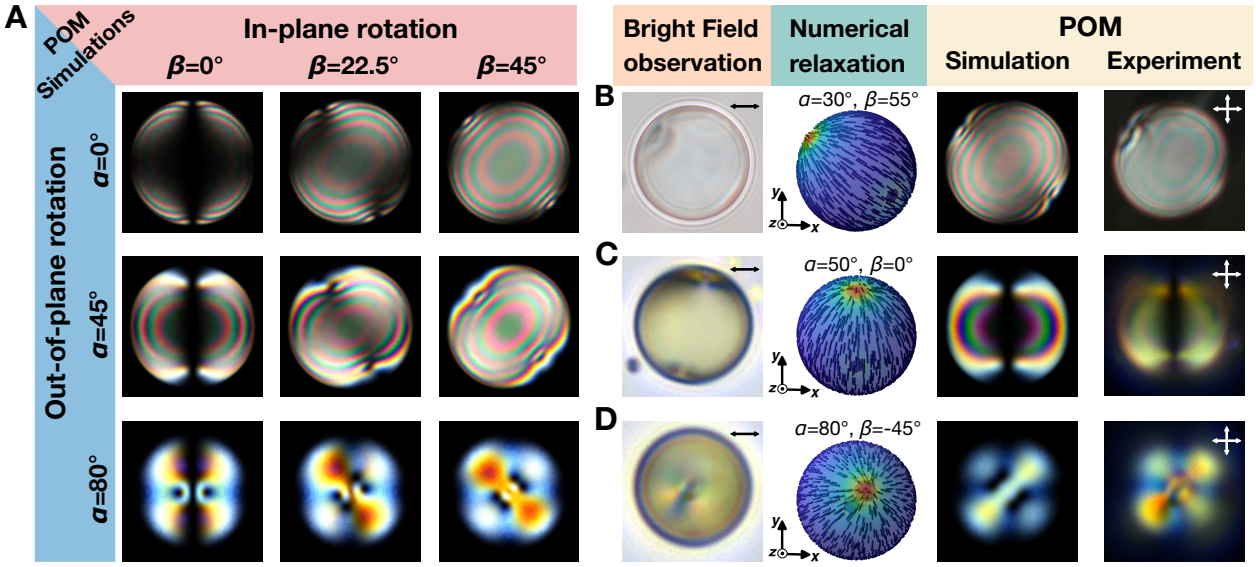

Figure 4: **POM images of bipolar droplets with different configurations from simulations and experiments.** (A) Effects of varying the orientation of a bipolar droplet with $d = 20\mu$m. (B-D), from left to right: bright field image, order field from numerical relaxation, cross-polarized image, simulated POM image. (B) Droplet with a diameter of 22.9μm. The poles are oriented close to the xy-plane with a small out-of-plane tilt. The simulated image is produced with $\alpha = 30°$ and $\beta = 55°$. (C) Droplet with a diameter of 13.3μm with the bipolar axis coinciding with the y-axis. The simulated image is produced with $\alpha = 50°$ and $\beta = 0°$. (D) Droplet with a diameter of 12.4μm. The defects are located near the center of the xy-plane aligned with the z-axis. The simulated image is produced with $\alpha = 80°$ and $\beta = -45°$. POM images in C and D are computed by using the light spectrum in Fig. S1(B).

The bipolar droplets have two defects at opposite poles that obey the $D_{\infty h}$ symmetry; all the orientations in 3D can be described by the α and β angles from the previous section. Simulated POM images for different orientations of the bipolar droplet are presented in Figure 4A. In agreement with literature reports, simulated images at $\alpha = 0°$ consist of concentric rings where the brightness and the outline change as the sample is rotated in the xy-plane. Optical textures similar to these are commonly reported in experiments.[11,55,58] Subtle deviations in the optical texture are often related to a small tilt of the bipolar axis, *i.e.* the defects are tilted out of plane. For instance, it was found that the best agreement between simulations and experiments correspond to Figure 4B, where $\alpha = 30°$ and $\beta = 55°$. Note that the spacing between the pink and green rings and the distortion features near the defects

are all reproduced accurately. Interestingly, screening other orientations yields unfamiliar optical textures without the concentric rings. As such images have rarely been associated with bipolar configurations, we performed additional experiments to confirm the accuracy of LCPOM. Although textures with concentric rings are observed more often, morphologies corresponding to orientations with out-of-plane rotation $\alpha > 45°$ (Figure 4C-D) are also confirmed experimentally. It is possible that these textures are reported less frequently because they are difficult to classify. An alternative explanation is that bipolar droplets can adopt preferred orientations due to sedimentation or flow.[23] Nevertheless, the agreement between experiments and simulations suggests that LCPOM reliably generates POM images of bipolar droplets at arbitrary orientations, thereby providing a useful tool with which to interpret POM images and classify droplets that exhibit ambiguous optical morphologies.

LCPOM with a twist: cholesteric systems

Compared to nematics, cholesterics exhibit additional helical structures along the orientation of the director.[17,59] Depending on the droplet diameter, the helical pitch (p_0), and the surface interactions, cholesteric droplets can adopt complex internal morphologies and, as such, provide unique opportunities for engineering electro-optical and sensing devices.[35,60–62] The POM images of cholesteric droplets (especially those with homeotropic anchoring conditions) can be highly sensitive to the droplet orientation, sometimes making it difficult to infer the exact underlying structure. Here, we computed POM images of a cholesteric droplet with a number of turns of $N = 3.8$, and compared them to experimental images with $N = 3.4$ reported by Krakhalev *et al.*[29] The order field was obtained from a theoretically-informed Monte Carlo simulation with homeotropic boundary conditions, following the procedure of Palacio-Betancur *et al.*[62] The POM calculations are based on the material properties of the E7 mixture.[29,63] The images produced in this manner show excellent agreement with experiments (Figure 5).[29,30] Note that this match is only obtained when the birefringence is

scaled down by 40% compared to that of the nematic host (E7), implying that the introduction of chiral dopant and the local twist in director field may have led to a decrease in the birefringence, consistent with recent literature measurements.[64] Another possible reason is that the droplets dispersed in polymer films may be oblate, and hence the optical path difference could be overestimated when a spherical geometry is assumed.[29] To examine how the optical texture changes with droplet orientation, POM images were calculated at varying angles and compared with experimental results from Krahkhalev *et al.* (Supplementary Movie 3).[29] We found that a small change in the orientation can lead to distinctly different optical textures of the droplet, yet a good match with experimental results can be obtained when the orientation is set close to those reported in the original paper (Figure 5B). In general, controlling the orientation of cholesteric droplets is challenging in experiments, making it difficult to investigate the optical texture systematically. By generating high-fidelity color images of complex structures, LCPOM can help develop a better understanding of structure in confined cholesterics, which is needed for the design of advanced optical devices.

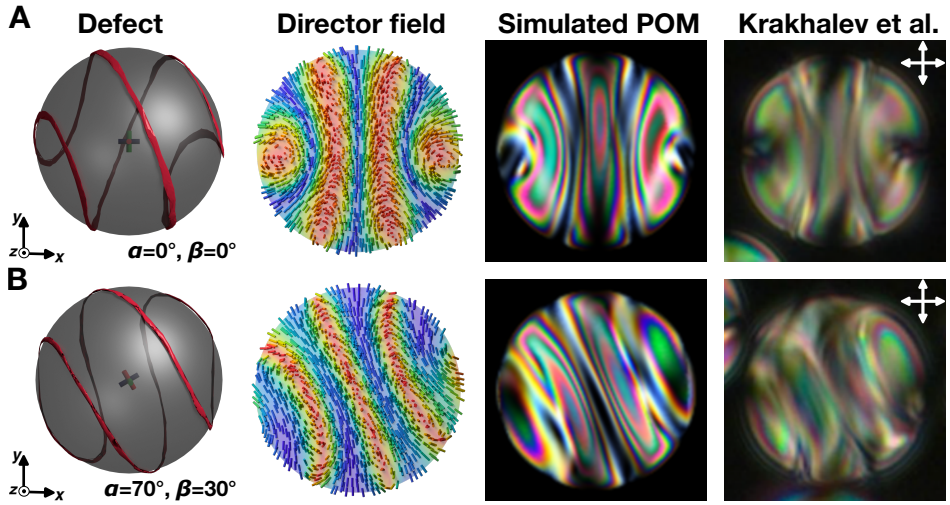

Figure 5: Comparison between simulated and experimental POM images of cholesteric droplets. The order fields of cholesteric droplets are obtained from Ginzburg-Landau relaxations with homeotropic boundary conditions. The number of turns is $N = 3.8$ and the diameter of the droplet is set to the experimental value of $d = 17\mu m$. From left to right: isoclinical lines in red, order field, simulated POM images, and experimental images. The experimental images of cholesteric droplets dispersed in a polymer film are adapted from Krakhalev *et al.* Scientific Reports (2017).[29] Order field in (B) is rotated by Euler angles $(\alpha, \beta) = (70°, 30°)$ relative to (A).

Extracting physical information of LC from POM data

Machine learning methods are revolutionizing microscopy analysis in the physical sciences, finding applications in denoising images, labeling features and revealing the underlying physics of complex systems.[65–68] Reports of their applications to microscopic images of LC systems to date mainly rely on the feature changes in the brightness profile while ignoring the information from the colors.[69,70] We anticipate that the LCPOM package will take the machine learning efforts one step further by aiding in generating training data with color information.

As demonstrated in the previous examples, the birefringence color depends sensitively on the order field and viewing angles of the droplet. In the following session, while not implementing a machine learning framework, we provide a benchmark study demonstrating that the color information can be utilized to determine the order parameter S as a function of temperature in confined droplet systems where feature changes are minimal. In this case, the vector field is treated as a radial hedgehog through different temperatures (T), but the scalar order parameter S is allowed to vary with T. This trivial case is chosen since the results can be compared directly with other measurement techniques, thereby providing some guidelines for future users regarding the accuracy and error of this method.

To begin with, radial droplets of 5CB in aqueous media are heated at a slow rate around 0.2 °C /min from 25°C to 35°C. In this process, a gradual color change indicative of decreasing average birefringence is observed up to the nematic-to-isotropic phase transition temperature (Figure 6A, See Supplementary Movie4 for the full dataset). To quantitatively interpret this color shift, experimental images are compared to a simulation reference dataset generated by LCPOM for a range of S values. To facilitate an automated comparison, an empirical decay profile near the edge of the droplet is used as a substitute for the Fresnel equation (Fig. S8), yielding images that closely resemble the experimental counterparts (Figure 6B). The S corresponding to each temperature is determined by searching for the image that has the highest similarity in color with the corresponding experimental image. To quantitatively

compare the color of experimental and simulated images, a pixel-wise comparison analogous to the root-mean-sqaure-error (RMSE) metric is implemented. Instead of measuring the distance on the RGB color space, the color difference is quantified by the CIEΔE (2000) metric for improved perceptual uniformity.[71] In the CIEΔE (2000) framework, a color difference of 100 indicates opposite colors such as red (RGB=(1,0,0)) and green (RGB=(0,1,0)) while a difference less than 2 indicates a close resemblance. The pixel-averaged color difference between the experimental image and the simulated images are shown in Figure 6C. (See Fig. S9). The candidates that possess the lowest color difference within an error of 1.5 are accepted. It is worth noting that this algorithm can reliably identify simulation images that closely align with human perceptual judgments (Figure 6C).

The same measurement and analysis are repeated for all the temperatures among a few droplets to determine S as a function of T (Figure 6D). Importantly, the measurements from individual experiments can be collapsed onto one curve within some error and the overall trend compares well with previous measurements by X-ray diffraction (XRD), optical and infrared (IR) techniques.[42,72,73] It is noted that the birefringence is $5 \sim 8\%$ lower than the literature data obtained in bulk. This discrepancy may arise from the confinement effects in the system or fluctuations due to hydrodynamic forces. In summary, this straightforward experiment demonstrates that one can extract meaningful physical properties of the nematic phase from the color information, enabled by the accurate dataset generated from the LCPOM simulations. We envision that by offering rich color information, LCPOM can bridge the gap between director information obtained from computer simulations and experimental microscopy images, hence making a key step towards data-driven analyses of the complex transitions and dynamics in liquid crystalline materials.

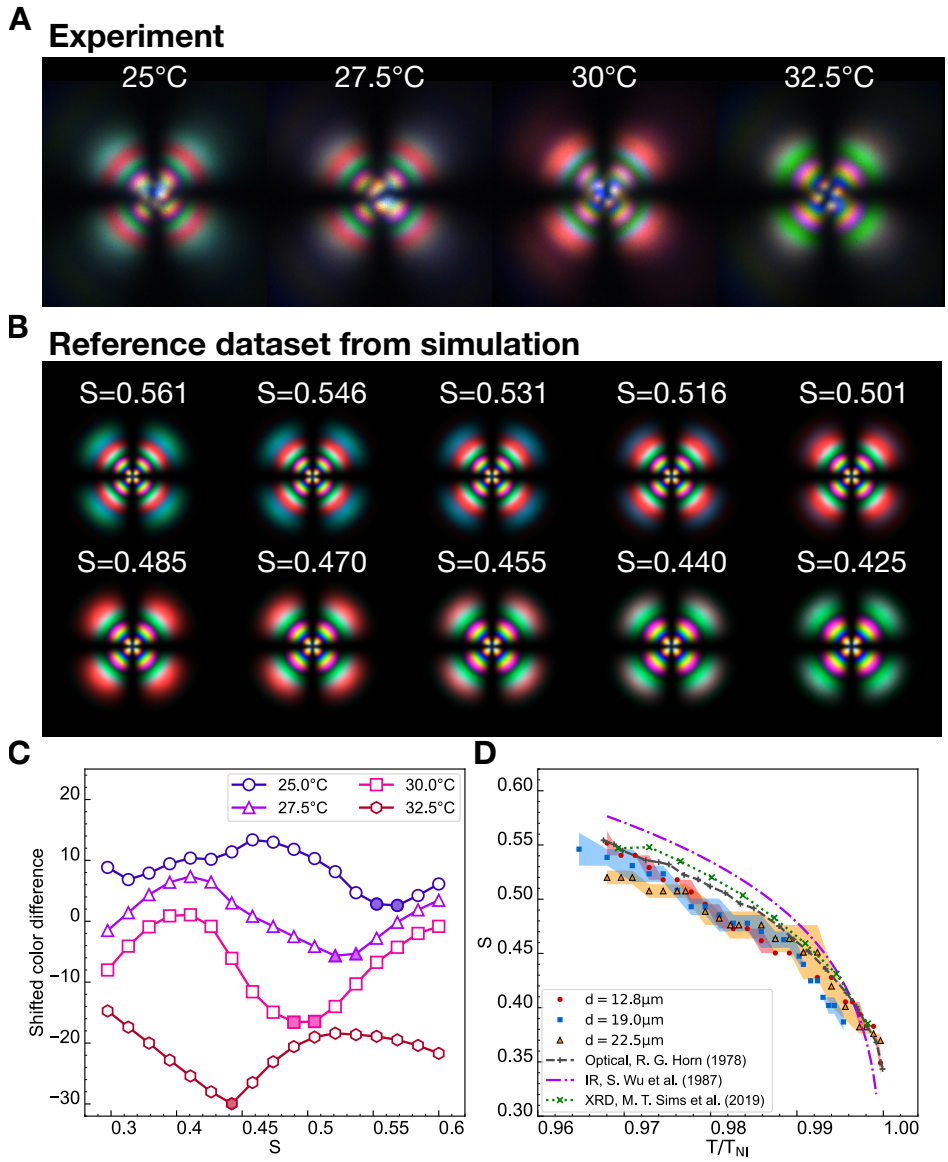

Figure 6: **Extracting order parameter S from images of radial droplets at varying temperatures.** (A) Experimental images of a radial droplet with $d_0 = 19.0\mu$m at varying temperatures. (B) Simulated images from a radial configuration with $d_0 = 19.0\mu$m. It is noted that varying S for d_0 is equivalent to varying d for the same S_0. Effectively, $S = d_0 \times S_0/d$. (C) Color differences measured by comparing the experimental images to each image in the reference dataset. The lines are shifted vertically by a constant for the ease of visualization. The solid symbols represent the identified matches. (D) The measured S as a function of normalized temperature T/T_{NI} for three different droplets are shown ($T_{NI} = 34.5$°C). Shaded area represents the range of S that meet the matching criteria. The results from this study is compared to literature measurements.[42,72,73]

Discussion and Conclusions

A method for simulation of color in POM images has been presented for confined liquid crystals, including droplets. By incorporating the emission spectrum of the light source, the dependence of refractive indices on wavelength, the transmission ratio at the droplet interface as well as the color matching functions, our simulation method is shown to be capable of generating colored POM images that are in quantitative agreement with experiments for radial, bipolar and cholesteric droplets. The method provides a particularly useful tool to validate theoretical models and to interpret experimental measurements. By comparing computed POM images of the order field profile obtained from simulations to experimental POM measurements, one can gain insights into the governing physics and the balance of various phenomenological parameters. Importantly, the new tools presented here provide a means of extracting important information, such as order parameters, that is hidden in the images and could not be easily determined using previously available monochromatic simulation techniques. We envision that the proposed computational tool will help generate a realistic dataset to aid machine learning efforts aimed at understanding the structure and dynamics of liquid crystals, and will help engineer a new generation of LC-based sensing devices where color is used to extract detailed information about molecular-level sensing events.

Acknowledgement

C.C. thanks Dr. Neil D. Dolinski for help with measuring the spectrum of the light sources. This work was primarily supported by the University of Chicago Materials Research Science and Engineering Center, which is funded by National Science Foundation under award number DMR-2011854. V.P.B. thanks the Fulbright commission in Colombia and COLCIENCIAS for support through the PhD student scholarship. M.S. is supported by National Science Foundation, Division of Materials Research, Condensed Matter Physics, under the

NSF CAREER award 2146428. The authors also acknowledge the Research Computing Center of the University of Chicago for computational resources.

Supporting Information Available

Experimental details, materials and further simulation details are provided in the Supplementary Information. The open-access LCPOM package and the user manual will be available at https://github.com/depablogroup/lc-pom upon publication. Other related data are included in LCPOM-Dataset.zip.

References

(1) Andrienko, D. Introduction to liquid crystals. *Journal of Molecular Liquids* **2018**, *267*, 520–541.

(2) de Gennes, P. G.; Prost, J. *The Physics of Liquid Crystals*, 2nd ed.; Clarendon Press, Oxford, 1993.

(3) Hernández-Ortiz, J. P.; Gettelfinger, B. T.; Moreno-Razo, J.; de Pablo, J. J. Modeling flows of confined nematic liquid crystals. *Journal of Chemical Physics* **2011**, *134*.

(4) Wu, S. A semiempirical model for liquid-crystal refractive index dispersions. *Journal of Applied Physics* **1991**, *69*, 2080–2087.

(5) Miller, D. S.; Carlton, R. J.; Mushenheim, P. C.; Abbott, N. L. Introduction to optical methods for characterizing liquid crystals at interfaces. *Langmuir* **2013**, *29*, 3154–3169.

(6) Miller, D. S.; Wang, X.; Abbott, N. L. Design of Functional Materials Based on Liquid Crystalline Droplets. *Chemistry of Materials* **2013**, *26*, 496–506.

(7) Chen, H. W.; Lee, J. H.; Lin, B. Y.; Chen, S.; Wu, S. T. Liquid crystal display and organic light-emitting diode display: present status and future perspectives. *Light: Science and Applications* **2018**, *7*, 17168.

(8) Carlton, R. J.; Hunter, J. T.; Miller, D. S.; Abbasi, R.; Mushenheim, P. C.; Tan, L. N.; Abbott, N. L. Chemical and biological sensing using liquid crystals. *Liquid Crystals Reviews* **2013**, *1*, 29–51.

(9) Mukherjee, F.; Shi, A.; Wang, X.; You, F.; Abbott, N. L. Liquid Crystals as Multifunctional Interfaces for Trapping and Characterizing Colloidal Microplastics. *Small* **2023**, 2207802.

(10) Lopez-Leon, T.; Fernandez-Nieves, A. Drops and shells of liquid crystal. *Colloid and Polymer Science* **2011**, *289*, 345–359.

(11) Shechter, J.; Atzin, N.; Mozaffari, A.; Zhang, R.; Zhou, Y.; Strain, B.; Oster, L. M.; de Pablo, J. J.; Ross, J. L. Direct Observation of Liquid Crystal Droplet Configurational Transitions using Optical Tweezers. *Langmuir* **2020**, *36*, 7074–7082.

(12) Martínez-González, J. A.; Zhou, Y.; Rahimi, M.; Bukusoglu, E.; Abbott, N. L.; de Pablo, J. J. Blue-phase liquid crystal droplets. *Proceedings of the National Academy of Sciences* **2015**, *112*, 13195–13200.

(13) Sadati, M.; Martinez-Gonzalez, J. A.; Zhou, Y.; Qazvini, N. T.; Kurtenbach, K.; Li, X.; Bukusoglu, E.; Zhang, R.; Abbott, N. L.; Hernandez-Ortiz, J. P.; de Pablo, J. J. Prolate and oblate chiral liquid crystal spheroids. *Science Advances* **2020**, *6*, 1–10.

(14) Lagerwall, J. P. F.; Scalia, G. A new era for liquid crystal research: Applications of liquid crystals in soft matter nano-, bio- and microtechnology. *Current Applied Physics* **2012**, *12*, 1387–1412.

(15) You, R.; Choi, Y.-S.; Shin, M. J.; Seo, M.-K.; Yoon, D. K. Reconfigurable Periodic Liquid Crystal Defect Array via Modulation of Electric Field. *Advanced Materials Technologies* **2019**, *4*, 1900454.

(16) Tomar, V.; Hernández, S. I.; Abbott, N. L.; Hernández-Ortiz, J. P.; de Pablo, J. J. Morphological transitions in liquid crystal nanodroplets. *Soft Matter* **2012**, *8*, 8679.

(17) Zhou, Y.; Bukusoglu, E.; Martínez-González, J. A.; Rahimi, M.; Roberts, T. F.; Zhang, R.; Wang, X.; Abbott, N. L.; de Pablo, J. J. Structural Transitions in Cholesteric Liquid Crystal Droplets. *ACS Nano* **2016**, *10*, 6484–6490.

(18) Norouzi, S.; Zhang, R.; Munguia-Fernández, J. G.; de Pablo, L.; Zhou, Y.; Taheri-Qazvini, N.; Shapiro, H.; Morin, S.; Martinez-Gonzalez, J. A.; Sadati, M.; de Pablo, J. J. Director Distortion and Phase Modulation in Deformable Nematic and Smectic Liquid Crystal Spheroids. *Langmuir* **2022**, *38*, 15272–15281.

(19) Concellón, A. Liquid Crystal Emulsions: A Versatile Platform for Photonics, Sensing, and Active Matter. *Angewandte Chemie International Edition* **2023**, *62*.

(20) Chen, K.; Hou, Y.; Chen, S.; Yuan, D.; Ye, H.; Zhou, G. Design, Fabrication, and Applications of Liquid Crystal Microlenses. *Advanced Optical Materials* **2021**, *9*.

(21) Chen, X. et al. First-principles experimental demonstration of ferroelectricity in a thermotropic nematic liquid crystal: Polar domains and striking electro-optics. *Proceedings of the National Academy of Sciences of the United States of America* **2020**, *117*, 14021–14031.

(22) Murphy, D. B.; Davidson, M. W. *Fundamentals of Light Microscopy and Electronic Imaging*; Wiley-Blackwell, 2012.

(23) Fernández-Nieves, A.; Link, D. R.; Márquez, M.; Weitz, D. A. Topological changes in bipolar nematic droplets under flow. *Physical Review Letters* **2007**, *98*, 1–4.

(24) Bellare, J. R.; Davis, H. T.; Miller, W. G.; Scriven, L. E. Polarized optical microscopy of anisotropic media: Imaging theory and simulation. *Journal of Colloid and Interface Science* **1990**, *136*, 305–326.

(25) Ondris-Crawford, R.; Boyko, E. P.; Wagner, B. G.; Erdmann, J. H.; Žumer, S.; Doane, J. W. Microscope textures of nematic droplets in polymer dispersed liquid crystals. *Journal of Applied Physics* **1991**, *69*, 6380–6386.

(26) Ellis, P. W.; Pairam, E.; Fernández-Nieves, A. Simulating optical polarizing microscopy textures using Jones calculus: A review exemplified with nematic liquid crystal tori. *Journal of Physics D: Applied Physics* **2019**, *52*, 213001.

(27) Jeong, J.; Davidson, Z. S.; Collings, P. J.; Lubensky, T. C.; Yodh, A. G. Chiral symmetry breaking and surface faceting in chromonic liquid crystal droplets with giant elastic anisotropy. *Proceedings of the National Academy of Sciences of the United States of America* **2014**, *111*, 1742–1747.

(28) Mur, U.; Čopar, S.; Posnjak, G.; Muševič, I.; Ravnik, M.; Žumer, S. Ray optics simulations of polarised microscopy textures in chiral nematic droplets. *Liquid Crystals* **2017**, *44*, 679–687.

(29) Krakhalev, M. N.; Gardymova, A. P.; Prishchepa, O. O.; Rudyak, V. Y.; Emelyanenko, A. V.; Liu, J. H.; Zyryanov, V. Y. Bipolar configuration with twisted loop defect in chiral nematic droplets under homeotropic surface anchoring. *Scientific Reports* **2017**, *7*, 2–11.

(30) Krakhalev, M. N.; Rudyak, V. Y.; Prishchepa, O. O.; Gardymova, A. P.; Emelyanenko, A. V.; Liu, J. H.; Zyryanov, V. Y. Orientational structures in cholesteric droplets with homeotropic surface anchoring. *Soft Matter* **2019**, *15*, 5554–5561.

(31) Mur, U.; Čopar, S.; Ravnik, M.; Čančula, M.; Žumer, S. Unveiling details of defect

structures in chiral and achiral nematic droplets by improving simulations of optical images. *Proc. Of SPIE* **2016**, *9940*, 99400V.

(32) Žumer, S.; Čančula, M.; Čopar, S.; Ravnik, M. Imaging and visualization of complex nematic fields. SPIE Proceedings. 2014; p 91820C.

(33) Geng, Y.; Noh, J.; Lagerwall, J. P. F. Transmission polarized optical microscopy of short-pitch cholesteric liquid crystal shells. *Proc. Of SPIE* **2016**, *9769*, 97690U.

(34) Máthé, M. T.; Buka, Á.; Salamon, P. Defects induced by anchoring transitions of nematic fluids at solid and gas interfaces. *Journal of Molecular Liquids* **2021**, *336*, 116074.

(35) Yoshioka, J.; Araoka, F. Topology-dependent self-structure mediation and efficient energy conversion in heat-flux-driven rotors of cholesteric droplets. *Nature Communications* **2018**, *9*, 1–11.

(36) Mollon, J. D. Color vision: Opsins and options. *Proceedings of the National Academy of Sciences* **1999**, *96*, 4743–4745.

(37) Fairman, H. S.; Brill, M. H.; Hemmendinger, H. How the CIE 1931 color-matching functions were derived from Wright-Guild data. *Color Research and Application* **1997**, *22*, 11–23.

(38) Broadbent, A. D. A critical review of the development of the CIE1931 RGB color-matching functions. *Color Research and Application* **2004**, *29*, 267–272.

(39) Wyman, C.; Sloan, P.-p.; Shirley, P. Simple Analytic Approximations to the CIE XYZ Color Matching Functions. *Journal of Computer Graphics Techniques* **2013**, *2*, 11.

(40) David, A.; Whitehead, L. A. LED-based white light. *Comptes Rendus Physique* **2018**, *19*, 169–181.

(41) Wu, S. Refractive index dispersions of liquid crystals. *Optical Engineering* **1993**, *32*, 1775.

(42) Horn, R. Refractive indices and order parameters of two liquid crystals. *Journal de Physique* **1978**, *39*, 105–109.

(43) Li, J.; Gauza, S.; Wu, S.-T. Temperature effect on liquid crystal refractive indices. *Journal of Applied Physics* **2004**, *96*, 19–24.

(44) Pedrotti, F. L.; Pedrotti, L. S. *Introduction to Optics*, 2nd ed.; Prentice-Hall Internation, Inc., 1993.

(45) Steinberg, S. Accurate Rendering of Liquid-Crystals and Inhomogeneous Optically Anisotropic Media. *ACM Transactions on Graphics* **2020**, *39*, 1–23.

(46) Walters, M.; Wei, Q.; Chen, J. Z. Y. Machine learning topological defects of confined liquid crystals in two dimensions. *Physical Review E* **2019**, *99*, 1–10.

(47) Doi, H.; Takahashi, K. Z.; Tagashira, K.; Fukuda, J.-i.; Aoyagi, T. Machine learning-aided analysis for complex local structure of liquid crystal polymers. *Scientific Reports* **2019**, *9*, 16370.

(48) Ramezani-Dakhel, H.; Sadati, M.; Zhang, R.; Rahimi, M.; Kurtenbach, K.; Roux, B.; de Pablo, J. J. Water Flux Induced Reorientation of Liquid Crystals. *ACS Central Science* **2017**, *3*, 1345–1349.

(49) Armas-Pérez, J. C.; Londono-Hurtado, A.; Guzmán, O.; Hernández-Ortiz, J. P.; Pablo, J. J. D. Theoretically informed Monte Carlo simulation of liquid crystals by sampling of alignment-tensor fields. *Journal of Chemical Physics* **2015**, *143*, 044107.

(50) Hernández, S. I.; Moreno-Razo, J. A.; Ramírez-Hernández, A.; Díaz-Herrera, E.; Hernández-Ortiz, J. P.; de Pablo, J. J. Liquid crystal nanodroplets, and the balance between bulk and interfacial interactions. *Soft Matter* **2012**, *8*, 1443–1450.

(51) Armas-Pérez, J. C.; Hernández-Ortiz, J. P.; de Pablo, J. J. Liquid crystal free energy relaxation by a theoretically informed Monte Carlo method using a finite element quadrature approach. *Journal of Chemical Physics* **2015**, *143*, 243157.

(52) Mkaddem, S.; Gartland, E. C. Fine structure of defects in radial nematic droplets. *Physical Review E* **2000**, *62*, 6694–6705.

(53) Terentjev, E. M. Disclination loops, standing alone and around solid particles, in nematic liquid crystals. *Physical Review E* **1995**, *51*, 1330–1337.

(54) Kleman, M.; Lavrentovich, O. D. Topological point defects in nematic liquid crystals. *Philosophical Magazine* **2006**, *86*, 4117–4137.

(55) Volovik, G.; Lavrentovich, O. D. Topological dynamics of defects: boojums in nematic drops. *Sov. Phys. Jetp* **1983**, *58*, 1159–1166.

(56) Lavrentovich, O. D.; Terentjev, E. M. Phase transition altering the symmetry of topological point defects (hedgehogs) in a nematic liquid crystal 0. *Sov. Phys. Jetp* **1987**, *64*, 1237–1244.

(57) de la Cotte, A.; Stenull, O.; Ettinger, S.; Collings, P. J.; Lubensky, T. C.; Yodh, A. G. Giant director fluctuations in liquid crystal drops. *Physical Review E* **2022**, *105*, 044702.

(58) Yang, C.; Chen, R.; Feng, L.; Zhang, R.; Chen, D. Electro-optic response of bipolar nematic liquid crystal confined in oblate spheroid. *Frontiers in Soft Matter* **2022**, *2*, 1–9.

(59) Prishchepa, O. O.; Zyryanov, V. Y.; Gardymova, A. P.; Shabanov, V. F. Optical Textures and Orientational Structures of Nematic and Cholesteric Droplets with Heterogeneous Boundary Conditions. *Molecular Crystals and Liquid Crystals* **2008**, *7*, 1740.

(60) Lee, H. G.; Munir, S.; Park, S. Y. Cholesteric Liquid Crystal Droplets for Biosensors. *ACS Applied Materials and Interfaces* **2016**, *8*, 26407–26417.

(61) Xiang, J.; Varanytsia, A.; Minkowski, F.; Paterson, D. A.; Storey, J. M. D.; Imrie, C. T.; Lavrentovich, O. D.; Palffy-Muhoray, P. Electrically tunable laser based on oblique heliconical cholesteric liquid crystal. *Proceedings of the National Academy of Sciences* **2016**, *113*, 12925–12928.

(62) Palacio-Betancur, V.; Armas-Pérez, J. C.; Villada-Gil, S.; Abbott, N. L.; Hernández-Ortiz, J. P.; de Pablo, J. J. Cuboidal liquid crystal phases under multiaxial geometrical frustration. *Soft Matter* **2020**, *16*, 870–880.

(63) Li, J.; Wen, C. H.; Gauza, S.; Lu, R.; Wu, S. T. Refractive indices of liquid crystals for display applications. *IEEE/OSA Journal of Display Technology* **2005**, *1*, 51–61.

(64) Zaplotnik, J.; Mur, U.; Malkar, D.; Ranjkesh, A.; Muševič, I.; Ravnik, M. Photonic eigenmodes and transmittance of finite-length 1D cholesteric liquid crystal resonators. *Scientific Reports* **2023**, *13*, 16868.

(65) Colen, J.; Han, M.; Zhang, R.; Redford, S. A.; Lemma, L. M.; Morgan, L.; Ruijgrok, P. V.; Adkins, R.; Bryant, Z.; Dogic, Z.; Gardel, M. L.; de Pablo, J. J.; Vitelli, V. Machine learning active-nematic hydrodynamics. *Proceedings of the National Academy of Sciences* **2021**, *118*, e2016708118.

(66) Alvarado, W.; Agrawal, V.; Li, W. S.; Dravid, V. P.; Backman, V.; de Pablo, J. J.; Ferguson, A. L. Denoising Autoencoder Trained on Simulation-Derived Structures for Noise Reduction in Chromatin Scanning Transmission Electron Microscopy. *ACS Central Science* **2023**, *9*, 1200–1212.

(67) Rivenson, Y.; Göröcs, Z.; Günaydin, H.; Zhang, Y.; Wang, H.; Ozcan, A. Deep learning microscopy. *Optica* **2017**, *4*, 1437.

(68) Melanthota, S. K.; Gopal, D.; Chakrabarti, S.; Kashyap, A. A.; Radhakrishnan, R.; Mazumder, N. Deep learning-based image processing in optical microscopy. *Biophysical Reviews* **2022**, *14*, 463–481.

(69) Sigaki, H. Y. D.; de Souza, R. F.; de Souza, R. T.; Zola, R. S.; Ribeiro, H. V. Estimating physical properties from liquid crystal textures via machine learning and complexity-entropy methods. *Physical Review E* **2019**, *99*, 013311.

(70) Sigaki, H. Y. D.; Lenzi, E. K.; Zola, R. S.; Perc, M.; Ribeiro, H. V. Learning physical properties of liquid crystals with deep convolutional neural networks. *Scientific Reports* **2020**, *10*, 7664.

(71) Sharma, G.; Wu, W.; Dalal, E. N. The CIEDE2000 color-difference formula: Implementation notes, supplementary test data, and mathematical observations. *Color Research and Application* **2005**, *30*, 21–30.

(72) Wu, S.-T. Infrared markers for determining the order parameters of uniaxial liquid crystals. *Applied Optics* **1987**, *26*, 3434.

(73) Sims, M. T.; Abbott, L. C.; Richardson, R. M.; Goodby, J. W.; Moore, J. N. Considerations in the determination of orientational order parameters from X-ray scattering experiments. *Liquid Crystals* **2019**, *46*, 11–24.

TOC Graphic

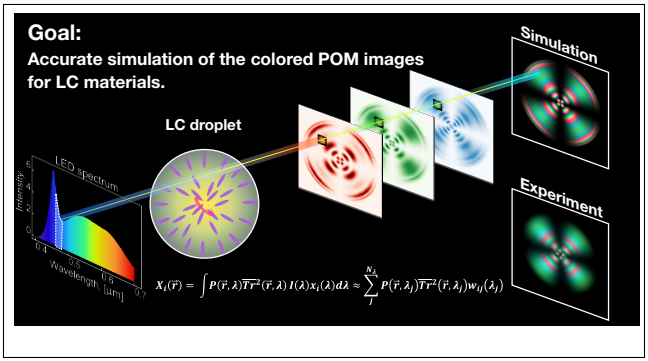
Goal:
Accurate simulation of the colored POM images for LC materials.
LC droplet
LED spectrum
Intensity
Wavelength [um]
Simulation
Experiment